Wall-wall and kink-kink interactions in ferroelastic materials

Guangming Lu,[1,*] Xiangdong Ding,[2] Jun Sun,[2] and Ekhard K. H. Salje[3,*]

[1]*School of Environmental and Material Engineering, Yantai University, Yantai 264005, China*

[2]*State Key Laboratory for Mechanical Behavior of Materials, Xi'an Jiaotong University, Xi'an 710049, China*

[3]*Department of Earth Sciences, University of Cambridge, Cambridge CB2 3EQ, United Kingdom*

(Received 2 June 2022; accepted 5 October 2022; published 20 October 2022)

Kinks interact with other kinks and antikinks elastically in ferroelastic domain walls and other interfaces in ferroic materials. In thin samples, suitable for transmission electron-microscopy, the interaction is purely dipolar with no indication of monopolar or higher order contributions. Kinks and antikinks attract each other while kink-kink interactions are repulsive. When the kinks are situated in two parallel twin walls, they display the same attraction/repulsion. We argue that this interaction constitutes, part or all, the elusive wall-wall interaction in ferroelastics. The dipolar interactions over distances d between the kinks and between walls decay as $1/d^2$ when the samples have some nanoscale size. Nanoscale samples bend and tilt when kinks are introduced with typical bent regions of some 1 nm and tilt angles of some 1.2°. Multiple kinks will enhance the effect systematically and bent and modulated twin walls are predicted.

DOI: 10.1103/PhysRevB.106.144105

I. INTRODUCTION

Pattern formation dominates applications of ferroelectrics, ferromagnets, and ferroelastics in device materials [1–4]. Field induced hysteresis is generated by the change of patterns under applied fields [5,6] and determines memory effects, piezoelectricity [7], elastic weakening [8], and avalanche behavior at high frequencies [9]. Typically, domain patterns [10] range from arrays of sparse domain boundaries [11] to dense fields of domains which usually form domain glasses [12]. Microscopically, domain patterns and related functional properties depend on the mobile atomic steps (kinks of atomic scale) inside ferroic domain boundaries, such as the two kinks in 90° domain wall in lead titanate (Fig. 1).

In most high-density domain patterns, the interaction between domain boundaries is well understood to stem from junctions between intersecting boundaries [15–19]. The resultant domain patterns are highly complex with the intersection of horizontal and vertical domain walls. Many studies focused on the question how this structural complexity influences the switching process [20]. Surprisingly, interactions even in the simplest configuration of domain boundaries, namely two parallel domain walls, is still not understood. This topic is of great importance to applications when domain boundary patterns are fully engineered [21] while being also of a great challenge to theoretical approaches. Two trivial effects are first identified to focus on the key challenge. The first obvious effect relates to wall nucleating under appropriate boundary conditions [22,23], which is at the core of the famous Kittel law when the domain periodicity scales as the square-root of the sample dimension [24]. The Kittel law is brought about by the energy scaling of the nucleation energy balanced by the self-energy of the wall [25]. As such, these approaches use global energy minimization and provide no further insight into the geometrical nature of wall-wall interactions. The second obvious mechanism applies when the interwall distances are comparable with those of the local strain fields of the walls. In this case the interaction energy of two adjacent walls is reduced by forming needle domains [15,26]. The needle tip is located according to the trade-off between the wall energy, the bending energy of the needle and the external boundary conditions [11,27]. Similar energy minimization strategies have been applied successfully for the analysis of exsolution patterns and emphasizes the fundamental role played by elastic stress interactions [28,29]. Global energy arguments have already been combined with more local structural arguments in Ref. [30] so that at least some rough ideas of the actual strain fields emerge from this approach. Nevertheless, no valid hypothesis how wall-wall interactions was generated in geometrical terms whereby parallel walls with distances larger than the wall thickness are supposed to be inert. This scenario is subject of our paper. More precisely, here we deal with the scenario where walls are separated beyond the wall thickness including local atomic relaxations inside the walls and large-scale shape changes of the sample. No external stress is applied. We focus on samples which can be imaged in transmission electron microscopy such as shown in Fig. 1, thus they are thin samples of nanoscale size.

The first progress in this field was due to Lajzerowicz and Levanyuk [31] who considered macroscopic electric fields arising from thermal fluctuations of two ferroelectric domain walls. They specifically investigated wall-bending of the domain boundary and the resulting electric dipoles which then interact between walls via Coulomb forces. The attraction energy of two parallel walls in this model decays at large distances d between two walls as d^{-2} with a

*Corresponding authors: luguangming1990@ytu.edu.cn; ekhard@esc.cam.ac.uk

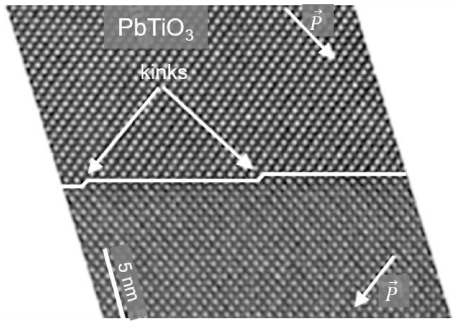

FIG. 1. Kinks in a 90° domain wall in lead titanate observed by high-resolution transmission electron microscopy (modified after Stadelmann [13,14]).

prefactor that is proportional to temperature and to a ratio of dielectric constants that is equal to unity for an isotropic medium. All distances are considered bigger than the wall thickness w. Other decay exponents were observed to range from -1 to -4, as described in Ref. [31]. The exponent -2 is valid for proper ferroelectrics and improper ferroelectrics with a quadratic dependence of the spontaneous polarization on the order parameter. They also argued that van der Waals interactions are weaker than the bending-bending interaction and do not contribute significantly. For nonferroelectric, nonferroelastic, nonferromagnetic domain walls, the power-law fluctuation-induced attraction is postulated. Subsequently, Salje and Vallade showed that this argument needs to be modified in case of elastically strongly anisotropic interactions [32]. The outcome of this research in the 1990s was hence that power law interactions are expected for interwall interactions in ferroelectrics but, unfortunately, still no detailed structural properties of the interaction mechanism could be obtained from this approach. Furthermore, it is now known that ferroelastics, which are not ferroelectric, usually contain large electrical dipoles in the twin walls, but not in the bulk [17,33–36] so that the electric dipole-dipole interaction will contribute to domain wall bending (sometimes coined "arching"). This idea supports [37] a quasi-Rayleigh model which was proposed to describe the hysteresis behavior of piezoelectric actuators (PEAs) and piezobased systems. Local wall bending and arching [38,39] were also observed by mechanical spectroscopy [8]. The question then arose how exactly the wall bending occurs on an atomic scale.

The role of boundaries and relaxation of the sample was emphasized in a series of papers during the same time. Computer simulation demonstrated that freely relaxing samples showed domain patterns different from constrained samples, i.e., different boundary conditions [40–43]. These arguments became even more important when nanoparticles and small samples are systematically investigated. Domain patterns deform the sample and simulations of clamped samples systematically miss this sample deformation. It is, therefore, crucial that all simulations are performed with open boundary conditions (stress-free surfaces) to allow the samples to deform. We will show in this paper that such deformations have a significant influence on the patterns even of surprisingly large samples.

A further approach emerged in 2017 when it was first proposed that wall bending may induce kinks in domain walls [44]. Furthermore, the kinks residing inside domain walls are not necessarily static but accelerate beyond the speed of sound under even modest external shear stress. The same kinks were subsequently found to be at the core of domain switching in metals [45,46] and during interactions with wall junctions which determine much of the mechanical properties of ferroelastic materials [47]. A typical example is shown in Fig. 1 where two kinks have a spacing of around 16 lattice units. Very high kink concentrations exist also in domain walls in uniaxial ferroelectrics like $LiNbO_3$ [48]. The twin wall has often mirror symmetry (in so-called **w** walls, Ref. [11]). The mirror symmetry is broken by kinks and local stress fields lead to significant strains emanating from the kinks. It is the purpose of this paper to characterize the strain fields and to show that strain-mediated interactions between kinks is a likely source for the interaction between parallel domain walls [49–52].

A step forwards was achieved in 2000 when Pertsev *et al.* [53] calculated equilibrium shapes of curved ferroelastic domain walls in crystals. Smooth kinks in walls were investigated using their dislocation-disclination model on the basis that the domain walls are infinitely narrow. They found that elastic monopoles (the interaction energy decay as $1/d$, where d is the kink-kink distance) exist in the bend regions of a wall although these authors already evoke the role of disclination dipoles for specific geometrical configurations. One of the main issues was, thus, to test the existence of monopolar elastic interactions in our limit of atomic-scale kinks in thin samples where strong lattice relaxations occur locally near the kink and in long-range interactions which modify the sample shape. After sufficient relaxations using realistic interatomic potentials, we found no monopolar interactions and an almost complete dominance of dipolar interactions.

II. THE MODEL

Ferroelastic patterns are described by a well-established model for ferroelastic transitions based on a double-well potential [4,20]. The construction of present two-dimensional atomic spring model is based on one Landau spring and two elastic springs, as schematically shown in Fig. 2. The potential energy $U(r)$ contains three terms, i.e., the harmonic first-nearest atomic interactions $U(r) = 20(r-1)^2$ (black springs), the anharmonic second-nearest interactions $U(r) = -25(r-\sqrt{2})^2 + 20000(r-\sqrt{2})$ (yellow springs) along diagonals in the lattice unit and the fourth-order third-nearest interactions $U(r) = 8(r-2)^4$ (green springs), where r is the distance between atoms. The first- and third-nearest interactions are related to the elastic interactions in ferroelastic materials. Landau spring represents a double-well potential of the ferroelastic transition with an equilibrium shear angle of 2°. The construction of this 2° shear angle was inspired by the well-known second-order phase transition of $SrTiO_3$ at 105 K. The initial twin angle is set to 2° by the second-nearest double-well potential but changes very slightly after relaxation. Similar atomic potentials can be found in our previous work [54].

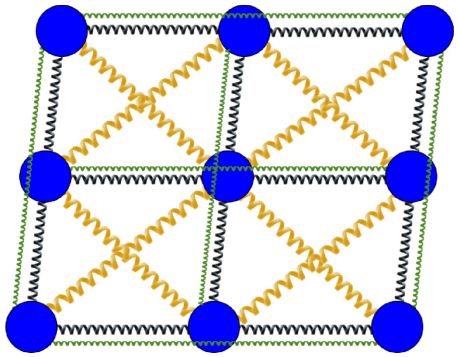

FIG. 2. Interatomic potential for generic ferroelastic model. The model with nearest-neighbor (black springs), next-nearest-neighbor (yellow Landau springs), and third-nearest-neighbor (green springs) interactions. This model ensures an appropriate shear angle with respect to the cubic unit cell.

In order to fully capture the lattice distortions induced by kinks, free or open (Dirichlet) boundary conditions are adopted in both x and y directions, which allows the samples to relax including shape changes and rotations. No external stress is applied. We set the equilibrium lattice parameters in x and y directions before relaxation to $a = 1$ Å, the relaxed single crystal lattice parameter is 1.0001297 Å in x direction and 0.9995027 Å in y direction for a sample size of 600 l.u.×201 l.u. (l.u. = lattice unit). The atomic mass is $M = 50$ amu. Several different initial simple ferroelastic patterns with one or two domain walls are constructed to study the single kink profile, kink-kink, and kink-antikink interactions. The kinks were initially created inside domain walls. The system was then relaxed using a conjugate gradient method. This is followed by 5×10^6 (5×10^3 ps) molecular dynamics (MD) simulation steps to obtain the full ferroelastic domain pattern. Ferroelastic domain patterns were obtained by extracting structural snapshots every 1000 MD steps (1ps) and averaging these patterns. In order to avoid the movement of kinks in the twin wall, the temperature of the simulation was kept very low at $T = 0.001$ K. The sample temperature was controlled by using Nose-Hoover thermostat method [55,56]. All simulations are performed using the LAMMPS code [57]. Visualizations are performed using the OVTIO software [58].

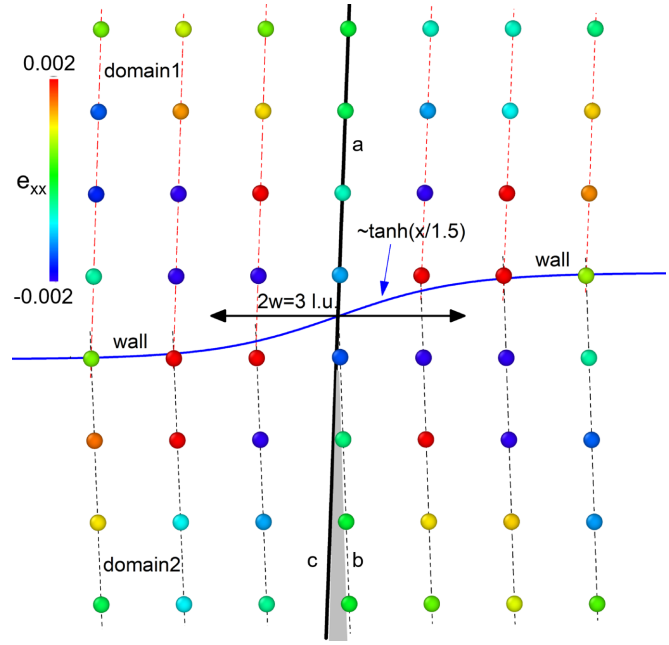

FIG. 4. Kink profile plotted as compatibility line between adjacent domains. Dashed lines represent the fitting lattice planes in domain 1 (red) and domain 2 (black). The kink profile follows a $\sim$ tanh (x/w) profile with $w = 1.5$ lattice units. The atoms are coded by atomic strain e_{xx}.

III. RESULTS

A. Static kink profiles

We construct a simple domain pattern with a size of 600 l.u.×201 l.u., which contains one horizontal domain wall located along the y direction. A static kink (Fig. 3) is initiated at the domain wall, as shown in the inset of Fig. 3. This configuration was then relaxed for 1×10^4 ps.

Figure 4 shows the local profile around this kink by extrapolating the lattice planes of both domains into the regime of the other domain. The intersection points of the lattice planes in the two domains define the compatibility between the lattice planes and hence the loci of the kink. The kink profile follow the analytical form $\sim$ tanh (x/w) where the kink thickness w is 1.5 l.u. (see the blue lines in Fig. 4) [59]. The vertical lattice plane in the middle of the kink is shown as black line a in

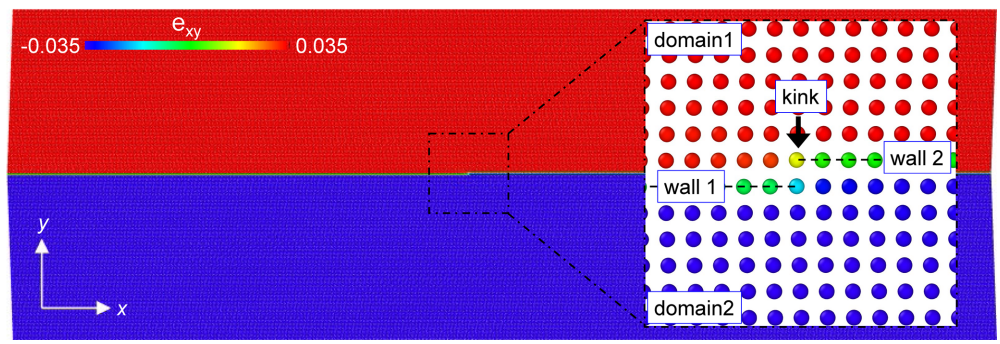

FIG. 3. Atomic image of a static kink residing inside a horizontal ferroelastic domain wall. The colors are coded by the atomic shear strain (e_{xy}). Green atoms in the inset (indicated by dashed lines) represent the domain walls with a kink.

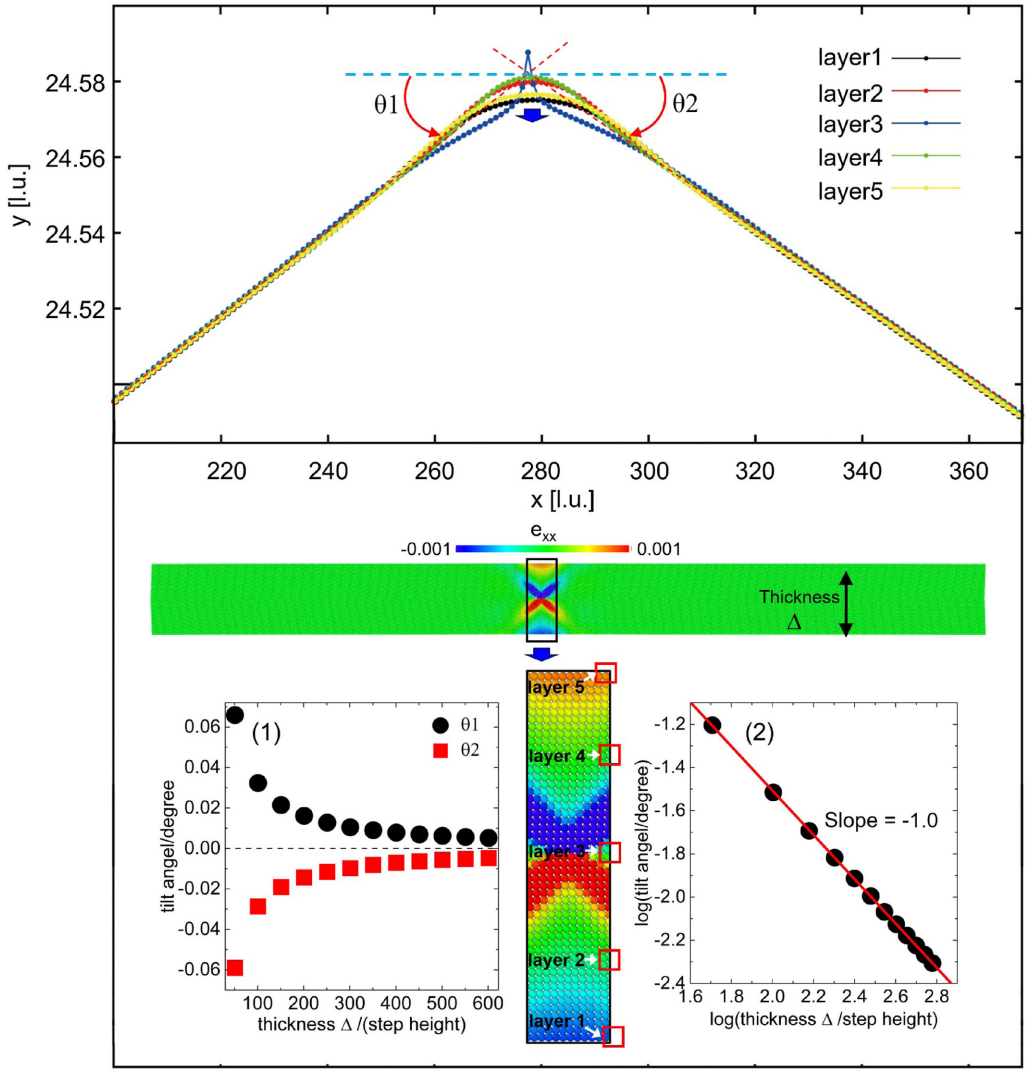

FIG. 5. Macroscopic deformations of sample with a static kink inside the horizontal domain wall. The strain map is coded by the strain component e_{xx}. The sample size is 51 l.u. in the y direction. Red dashed lines represent the fitting positions of lattice points on left and right of the middle kink. The angles between the horizontal direction and the tilted walls characterizes the tilt angles of the left and right end of the sample ($\theta 1$ and $\theta 2$). Layer1-layer5 represent different atomic layers of the sample from bottom surface to top surface. Inset (1) shows the macroscopic tilt angle as a function of sample thickness in the y direction, inset (2) shows the scaling exponent between the sample thickness and the tilt angle.

Fig. 4. The shear angle of the upper domain deviates from the lattice plane in the lower domain, the shear angle defines the twin angle, i.e., a wedge (grey shadow in Fig. 4) between the extrapolated lattice plane in domain 1 and the lattice planes in domain 2 (and vice versa). Two additional changes of the patterns were observed due to the open boundary conditions. Firstly, the entire sample weakly rotates after relaxation. Secondly, surface relaxations occur at all surfaces and lead to the twisting of the sample of such small size.

We observed the macroscopic bending correlated with kink-induced distortion in thin samples when comparing the systems with and without kinks [60]. While the twin wall in the sample without kinks is strictly horizontal, the twin wall in the kink system is bent. Figure 5 shows the left and right segment of the tilted twin wall, where the middle section near the kink is bent locally. The tilt angle is defined as the macroscopic angle between the twin wall at locations away from the kink and the horizontal direction ($\theta 1$ and $\theta 2$ along x direction in Fig. 5). Five atomic layers from the bottom to top surfaces [60] are selected to determine the positions of lattice points in the x direction. The kink inside the domain wall locally bends the lattice planes and curved lattices on top and bottom sides of domain wall (see enlarged region in Fig. 5). Left and right parts of a sample tilt by $\pm 0.066°$ on the left and right side of the sample (size of 51 l.u. in the y direction, see the lattice positions and strain maps in Fig. 5). All atomic layers from the bottom to top surface show similar tilt angles. Figure 5 shows the five layers next to the twin walls with the same tilt behavior but different bending behavior. This is compared with the construction in Fig. 4 where the middle vertical lines (indicated by a and b) are strain free besides the middle two atoms. When the upper middle lines (line '1') was extrapolated to the domain 2, the triangular wedge appears

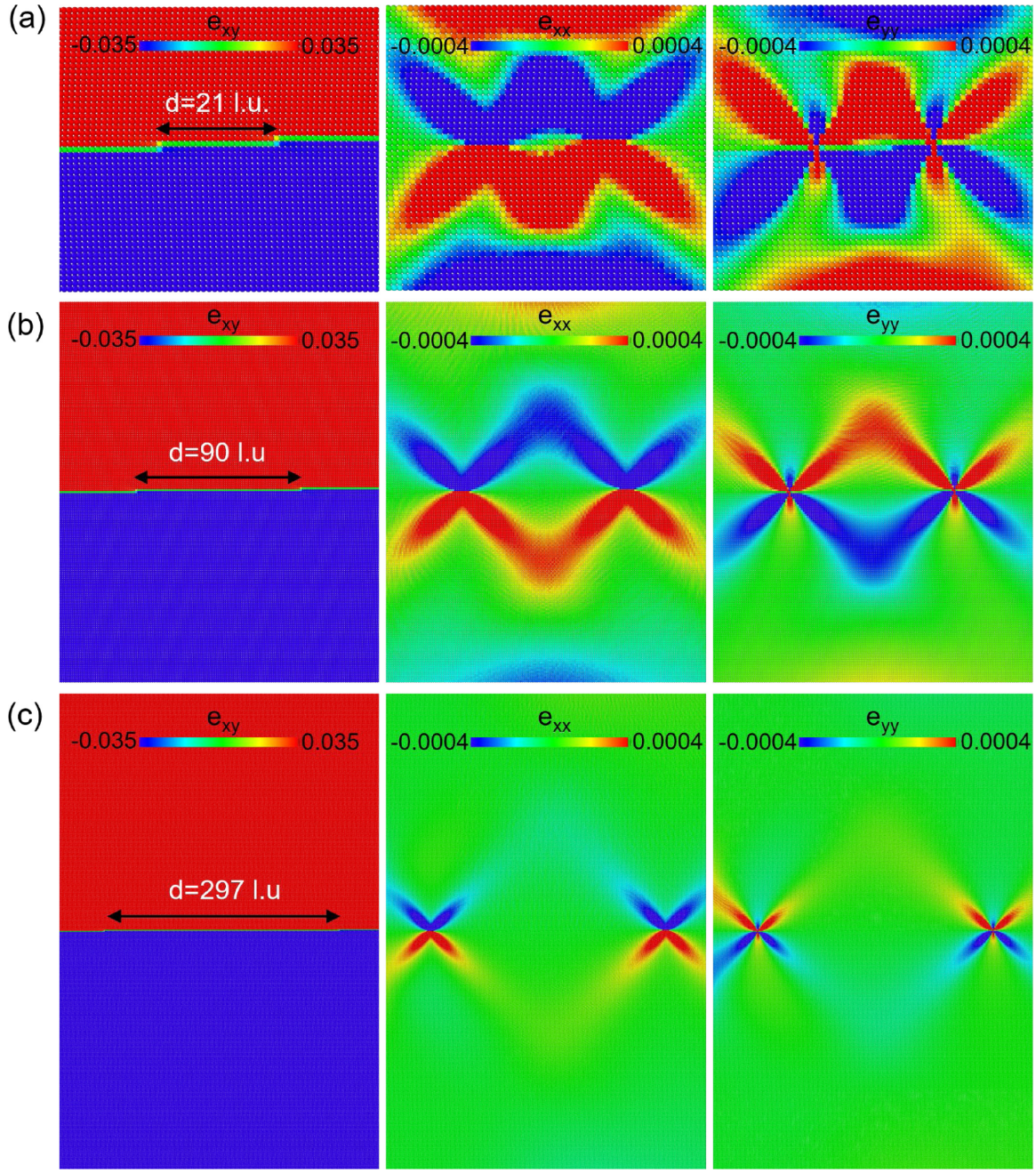

FIG. 6. Strain maps of kink-kink configurations inside horizontal wall with equilibrium separation distances resulting from repulsive interactions between kinks. The system sizes in y direction are 51 l.u. in (a), 201 l.u. in (b) and 601 l.u. in (c). Strain color maps are coded by atomic-level normal strains (e_{xx} and e_{yy}) and shear strain (e_{xy}).

between line 'c' and the dotted line for the atomic position (line 'b'). To comply with local compatibility, the triangular wedge is pushed upwards like the treatment of 90° corners in ferroelastic domains [15] which closes the gap and twists the domain walls downwards. This effect is strongly dependent on the sample size. Tilt angles of samples with dimensions of the y direction between 51 and 601 l.u. are shown in the inset in Fig. 5. The tilt angles θ decrease as the system thickness Δ (size perpendicular to horizontal wall, y direction) increases along the direction perpendicular to the domain walls [inset (1)] as $\theta \sim \Delta^{-1}$ [inset (2)].

B. Kink-kink and kink-antikink interactions in a twin wall

We now consider two interacting kinks inside the same twin wall (Fig. 6). The interaction is attractive for kink-antikink motions (with kink amplitudes in opposite directions) and repulsive for kink-kink configurations (with kink amplitudes in the same direction). When a kink-kink configuration is initialized inside the wall, the repulsive interactions moves the two kinks apart from each other to reduce the global energy.

The interaction energy of two kinks in the twin wall is now analyzed for 23 kink-kink configurations with a separa-

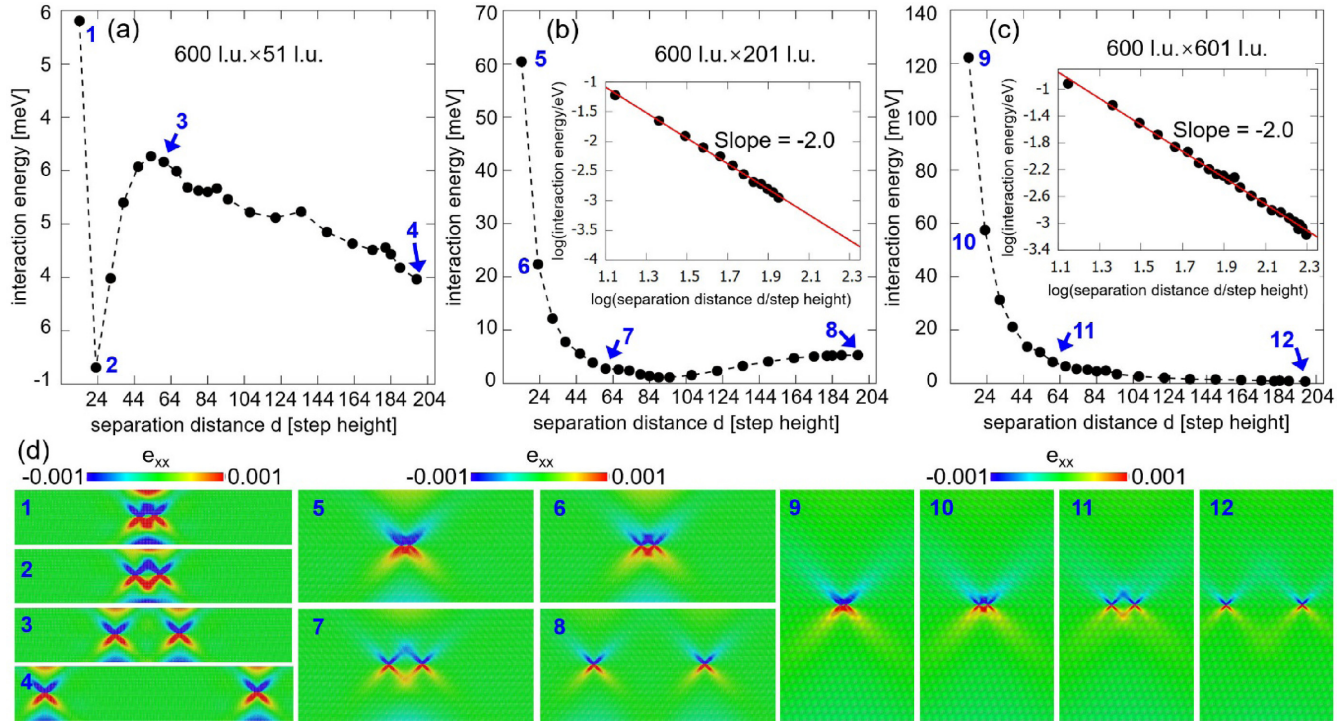

FIG. 7. Interaction energy of kink-kink configurations as a function of their separation distance. The system sizes in (a), (b) and (c) are 600 l.u.×51 l.u., 600 l.u.×201 l.u., and 600 l.u.×601 l.u.. 1–12 in (a)–(c) indicate the interaction energy of kink-kink configurations with separation distances of 14 l.u., 23 l.u., 60 l.u. and 198 l.u. (d) the corresponding strain maps for each configuration. Insets in (b) and (c) show the scaling $\Delta E \sim d^{-2}$ between the interaction energy and the kink-kink separation distance. Colors are coded according to the atomic-level normal strain e_{xx}.

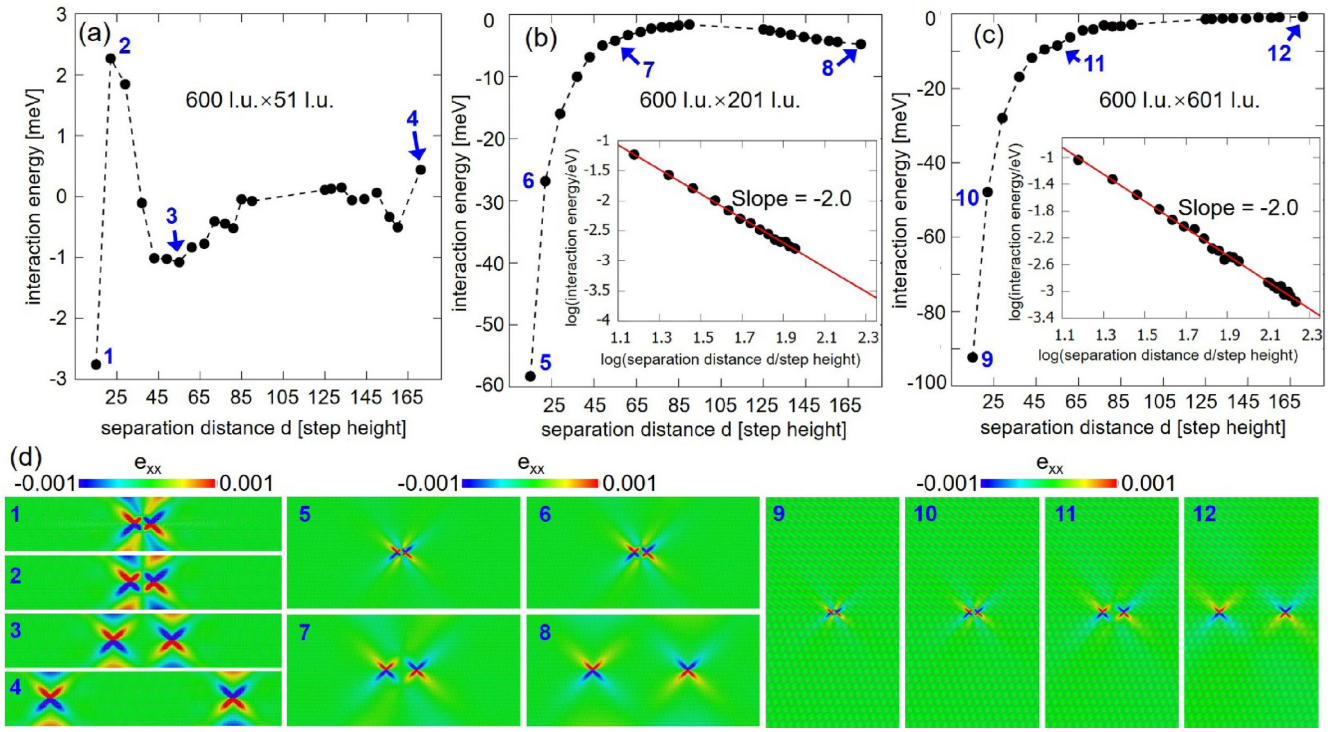

FIG. 8. Interaction energy between kink and antikink as a function of interkink distances. The system size in (a), (b) and (c) is 600 l.u.×51 l.u., 600 l.u.×201 l.u., and 600 l.u. × 601 l.u.. 1–12 in (a)–(c) indicate the interaction energy for distances of 15 l.u., 22 l.u., 55 l.u. and 171 l.u.. (d) The corresponding strain maps. Insets in (b) and (c) show the scaling $\Delta E \sim d^{-2}$ between the interaction energy and the kink-antikink separation distances. Colors are coded by atomic-level normal strain e_{xx}.

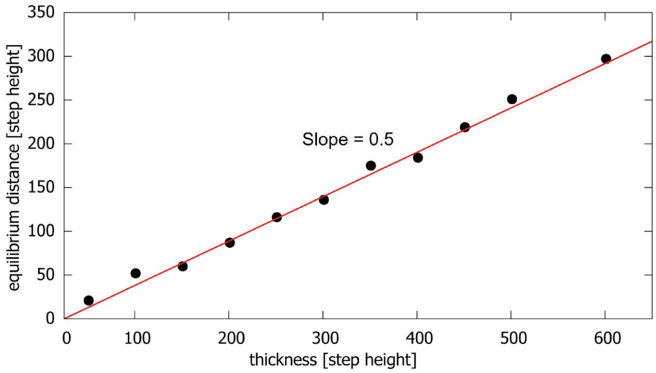

FIG. 9. Equilibrium kink-kink distances *versus* sample thickness in the *y* direction.

tion distance ranging from 14 to 198 l.u. in different system sizes with 51, 201, and 601 l.u. along *y* direction. For each configuration, we relax the system for 5×10^3 ps. A relaxation with a period of 5×10^3 ps was used to calculate the averaged potential energy, as shown in Fig. 7.

To calculate the interaction energy of the kink-kink configuration, the total potential energy is reduced by the potential energy of two noninteracting kinks. The kink-kink distance shows first a decrease when the distance is smaller than the equilibrium distance, and then increases [Fig. 7(a)] when surface strains in numbers 1–4 in Fig. 7(d) dominate. When the sample thickness in *y* direction extends to 201 l.u., a smooth potential energy minimum in Fig. 7(b) occurs at an interkink distance of. 90 l.u. The interaction energy follows a typical dipole-dipole interaction for distances smaller than the equilibrium distance. The scaling exponent is -2 for this interaction energy $\Delta E \sim d^{-2}$ [see inset in Fig. 7(b)]. For a system size of 601 l.u. in the *y* direction, a wider scaling regime is found with the same scaling exponent of -2 [see Fig. 7(c)]. The size effect (surface strains) is very large in small system, and strongly affects the kink-kink interaction energy while it is irrelevant for large system sizes. The crossover is at sizes equivalent to around 200 nm which shows that nanoparticles are prone to size effects while large single crystals are not.

In contrast to repulsive kink-kink interactions, kink-antikink interactions are attractive inside twin walls. Figure 8 shows 23 kink-antikink configurations inside the domain wall with separation distances from 15 to 171 l.u. with all the parameters identical to the kink-kink interactions.

Like kink-kink interactions, strong size effects are observed for small systems [Fig. 8(a)]. The interaction energy increases as the separation increases [see Figs. 8(b) and 8(c)]. There exists an energy maximum for the system of

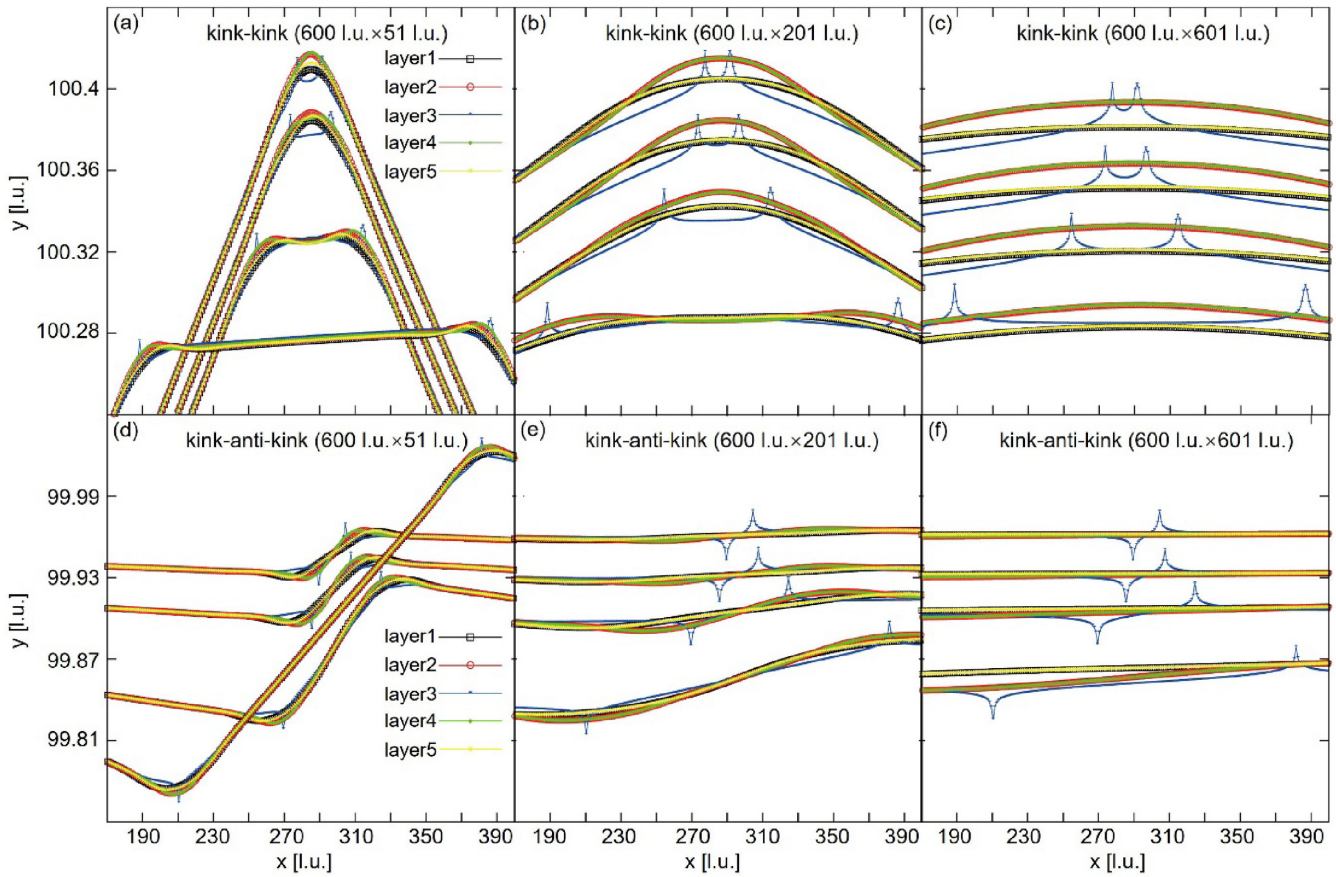

FIG. 10. Position of the twin walls near (anti-) kinks. The bents and tilts are induced by kink-kink pairs (a)–(c) and kink-antikink (d)–(f) pairs inside wall. The atomic layers (layer 1-layer 5) are the same as those in Fig. 4.

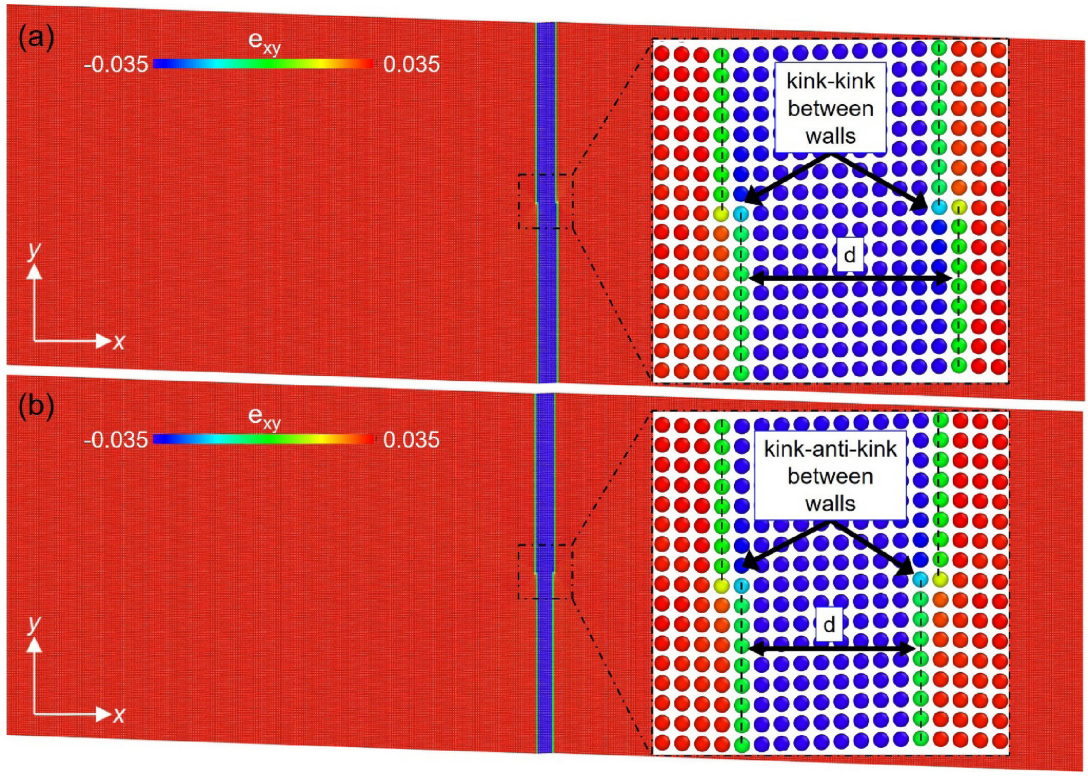

FIG. 11. Atomic structure of kink-kink (a) and kink-antikink (b) residing inside two parallel domain walls. The colors are coded by the atomic shear strain (e_{xy}). Green atoms (indicated by dashed lines) represent the domain walls with kinks in the insets.

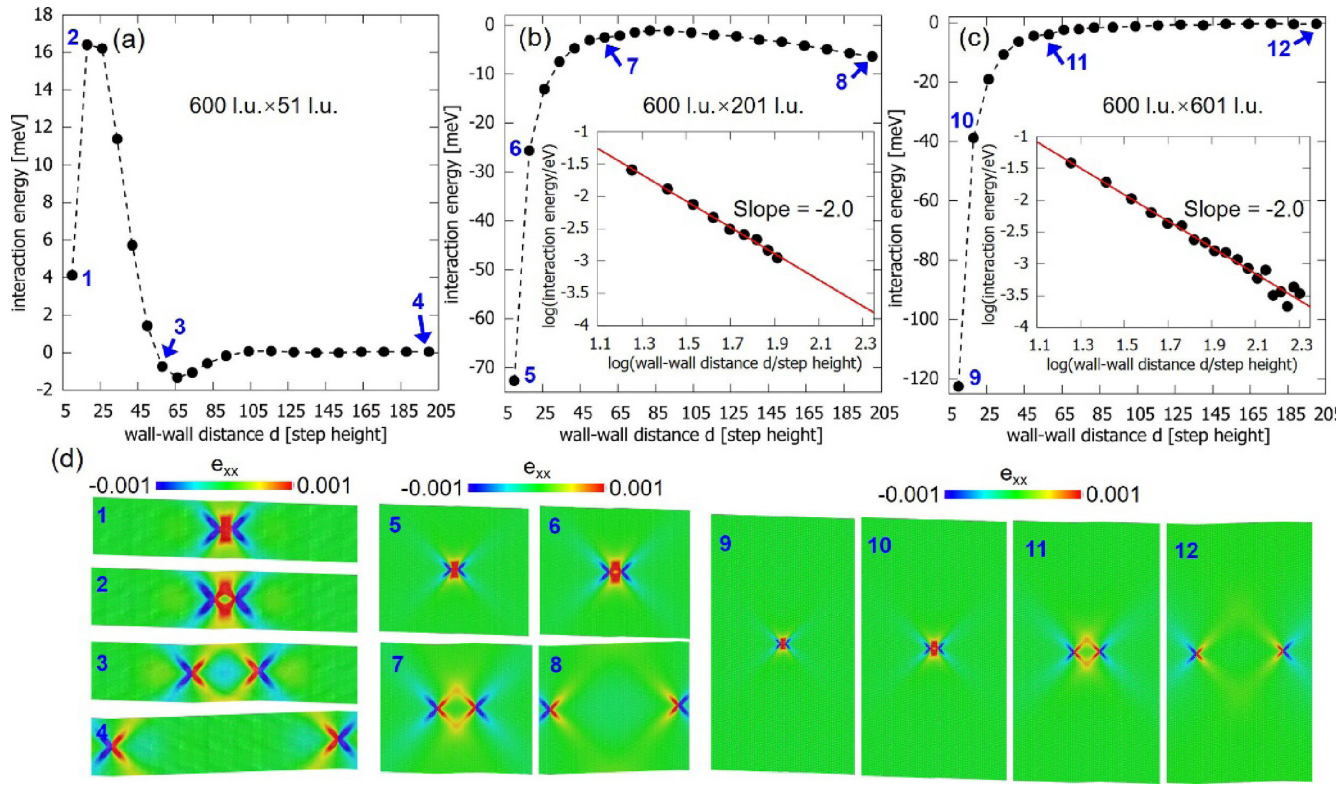

FIG. 12. Interaction energy of kink-kink configurations residing inside two parallel walls as function of wall-wall distances. The system size in (a), (b), and (c) are 600 l.u.×51 l.u., 600 l.u.×201 l.u., and 600 l.u.×601 l.u.. 1–12 in (a)–(c) indicate the interaction energy of kink-kink configurations with wall-wall distances of 10 l.u., 18 l.u., 58 l.u. and 200 l.u. (d) The corresponding strain maps for each configuration. Insets in (b) and (c) show the scaling exponent $\Delta E \sim d^{-2}$ between the interaction energy and the wall-wall distances. The colors are coded by atomic-level normal strain e_{xx}.

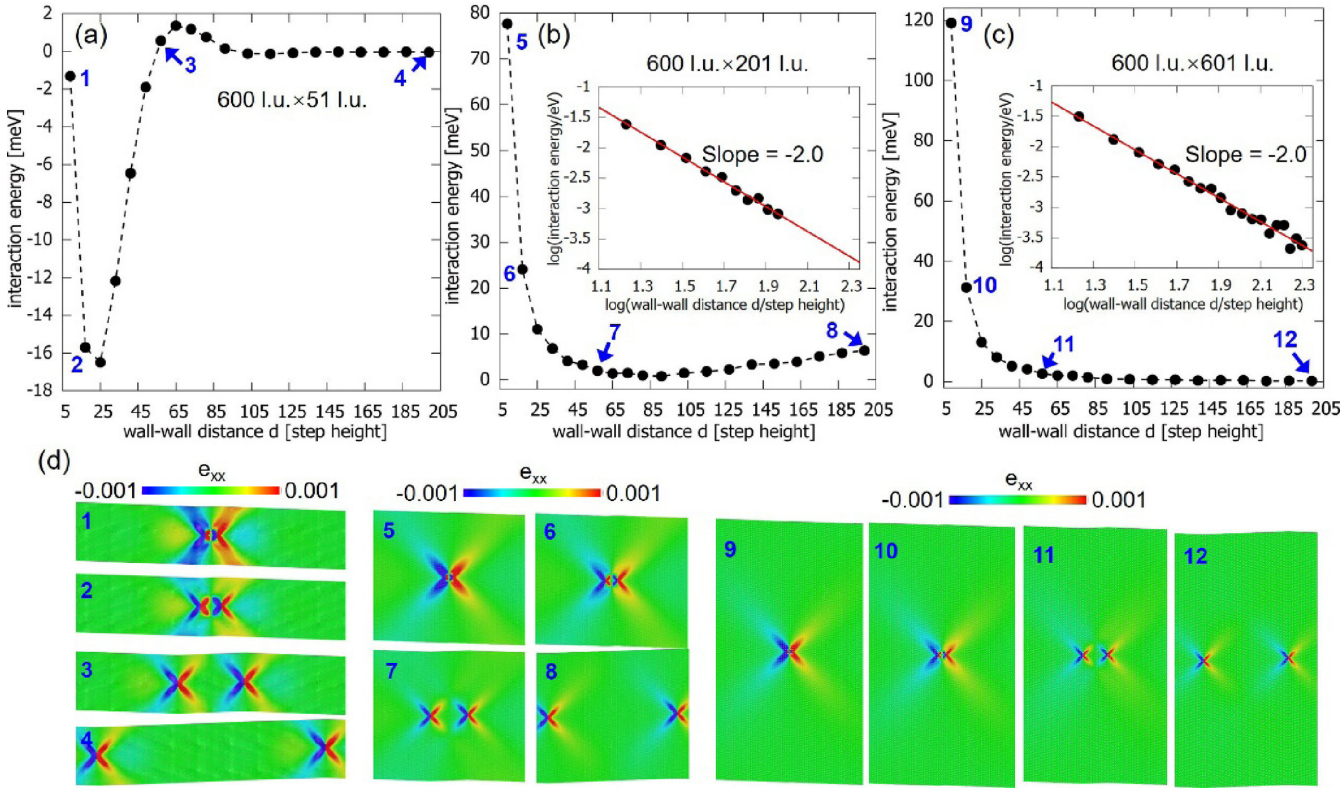

FIG. 13. Interaction energy of kink-antikink configurations residing inside two parallel walls as a function of wall-wall distances. The system size in (a)–(c) are 600 l.u.×51 l.u., 600 l.u.×201 l.u., and 600 l.u.×601 l.u. 1–12 in (a)–(c) indicate the interaction energy of kink-antikink configurations with wall-wall distances of 9 l.u., 17 l.u., 57 l.u. and 199 l.u.. (d) The corresponding strain maps for each configuration. Insets in (b) and (c) show the scaling $\Delta E \sim d^{-2}$ between the interaction energy and the wall-wall distances. The colors are coded by atomic-level normal strain e_{xx}.

600 l.u.×201 l.u. at distance of ∼90 l.u., below which the interaction energy follows the typical dipole-dipole interaction $\Delta E \sim d^{-2}$ with the same scaling exponent of −2 as the kink-kink configurations. A power-law interaction energy is also dominant in larger system of 600 l.u.×601 l.u. [see Fig. 8(c)].

We now analyze the equilibrium kink-kink configurations inside the horizontal wall with different thickness in the y direction when no Peierls pinning applies. To find the optimum positions for the kinks, we increase the temperature from 0.001 to 0.12 K. Figure 9 shows the equilibrium separations of kink-kink configurations after relaxations for 1×10^4 ps. The equilibrium distance for the system size is 21 l.u. when the size is 15 l.u. in the y direction, and increases to 90 and 297 l.u. when the system size was extended to 201 and 601 l.u.. Kink-kink configurations with sample thickness in the y direction between 51 and 601 l.u. show a linear relationship between equilibrium distances and sample thicknesses in the direction perpendicular to the domain wall with (equilibrium distance) ∼0.5 (step height) (Fig. 9).

Figure 10 shows the size dependence of the kink-kink and kink-antikink tilt configurations. The bending and the tilts become strongest for small sizes [Figs. 10(a)–10(c)]. The interkink region shows no tilting but some weak bending. The same singularities at the loci of the kinks are found for kink-antikink configurations in Figs. 10(d)–10(f). In contrast to the kink-kink scenario, the downwards tilt on the right end of the sample is now combined with an upwards tilt on the left side of the sample. The overall effect on the twin wall is, hence, that the wall remains overall straight but contains a double-bending region in between the two linear segments of the wall.

C. Kink interactions in parallel domain walls

Figure 11 shows the kinks and antikinks in parallel twin walls. Both structures consist of 600 l.u. layers in the x direction and 201 l.u. in the y direction. The wall is located the in the middle of the sample. After relaxation, two kinks (kink-kink and kink-antikink) remain stable at each domain wall (see insets in Fig. 11).

In order to study the size effects on the kink-kink interactions, we constructed three systems with different system sizes, i.e., 51, 201, and 601 l.u. along the y direction. For each system, the wall-wall distance ranges from 10 to 200 l.u. We created 20 different configurations to calculate the interaction energy with different wall-wall distances. Increasing the activation energy increases the mobility of the twin walls with the only interaction between the walls due to the kink-kink repulsion. At each configuration the interaction energy is obtained by subtracting the self-energy of the two kinks. Figure 12 shows the resulting interaction energy as a func-

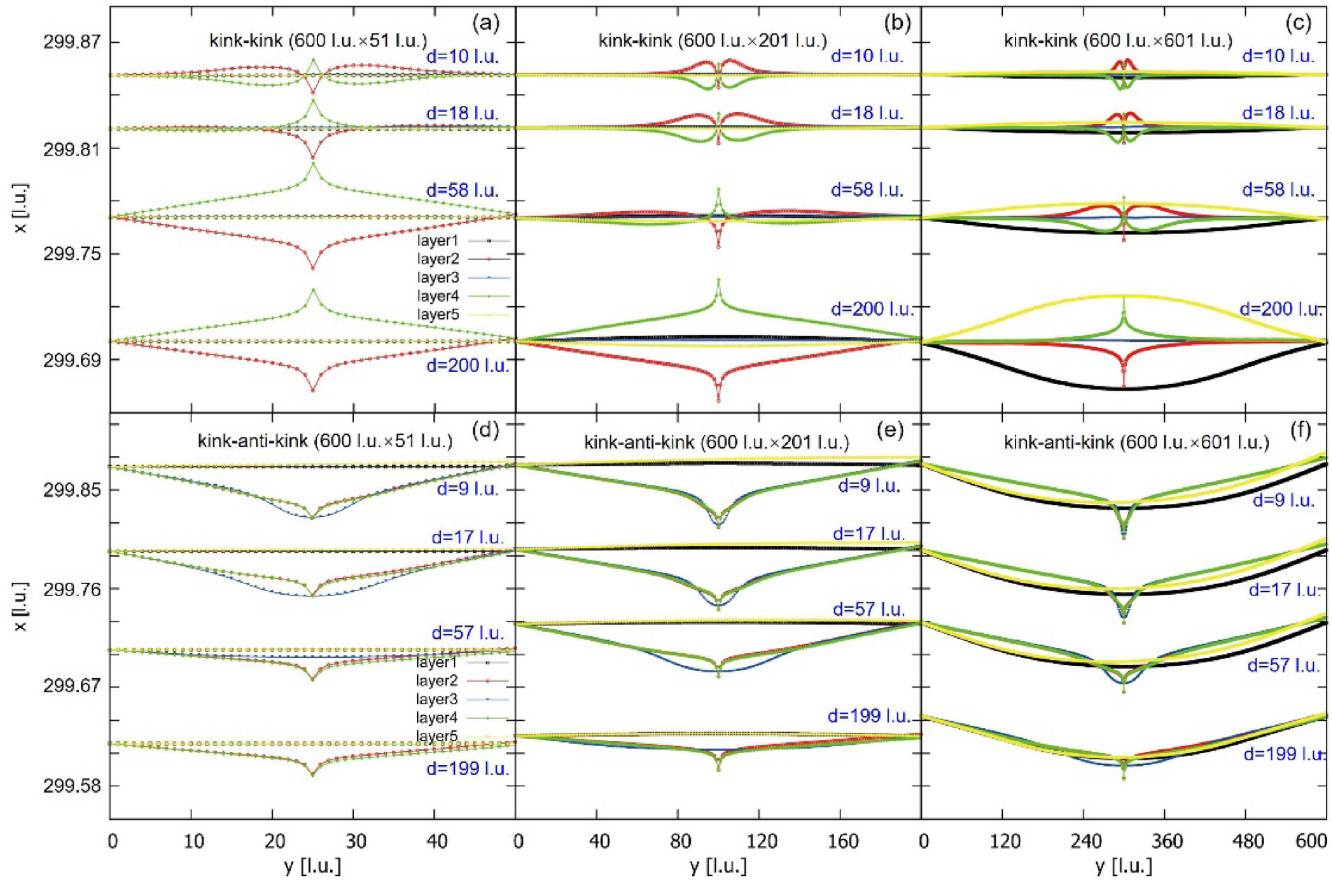

FIG. 14. Lattice deformation induced by kink-kink pair (a)–(c) and kink-antikink (d)–(f) pair inside two parallel walls. Layers numbered with 1 to 5 refer to the bottom surface layer, bottom twin wall layer, top twin wall layer, middle layer between two walls, and the top surface layer in the x direction. $d = 10$, $d = 18$, $d = 58$, and $d = 200$ in (a)–(c) are the wall-wall distances of different kink-kink configurations. $d = 9$, $d = 17$, $d = 57$, and $d = 199$ in (d)–(f) are the wall-wall distances of different kink-antikink configurations.

tion of the wall-wall distances. For sample sizes bigger than 51 l.u. along the y direction, the interaction energy degreases with increasing wall-wall distance as

$$E_{\text{w-w}} \sim d^{-2}.$$

This dipolar decay is the same as in the case of two kinks and kinks and antikinks in the same twin wall (see Figs. 7 and 8). The validity range of this simple dipolar interaction enhances for larger samples and covers most of the sample in the case of the largest samples of 600 l.u.×601 l.u., but not for the smallest sample of 600×51 l.u. While the maximum interaction energy is near zero with typical values near some 10 meV, i.e., not far from the typical wall energy, the interaction energy of the smallest sample displays a maximum of some 16 meV for distances of 25 l.u.. For such small samples, the strain fields are extremely strong at the sample surface [see numbers 1–4 in Fig. 12(d)] and no sample region on either side of the walls exists where the deformation is small. When the two walls repel each other, the macroscopic shape of the sample changes dramatically. Each twin wall leads to a local macroscopic bending of the sample with two twin walls leading to a zig-zag sample shape.

For kink-antikink initeractions, we consider three different system sizes of 51, 201, and 601 l.u. in the y direction. For each system size, 20 different kink-antikink configurations with wall-wall distances between 9 and 199 l.u. were constructed as the initial configurations. The sytem is then relaxed. Figure 13 shows the interaction energy between kink and antikinks as a function of wall-wall distances in different systems. Contrary to the kink-kink scenarios, the kink and antikinks attract each other [see Figs. 13(a)–13(c)]. For smaller systems, the surface strains dominate the interactions, and obvious strain patches can be found in numbers 1–4 in Fig. 13(d). As the system size increases along y direction, the size effect decreases, following a typical power-law decay $\Delta E \sim d^{-2}$ of the interaction energy in a system of 600 l.u.×201 l.u. [Fig. 13(b)]. A full range power-law decay is found in the larger system of 600 l.u.×201 l.u. with neglectable size effect. Figure 14 shows the size dependence of the kink-kink and kink-antikink tilt configurations.

IV. DISCUSSION

We demonstrated that all kink-kink interactions follow, for nanoscopic system sizes with full local atomic relaxations and macroscopic shape changes, dipole-dipole interactions without higher order quadrupolar or logarithmic corrections [61]. We find no monopolar interactions. Our results mirror previous results on the interactions between surface steps in vicinal surfaces [62,63]. The long-range elastic fields of

surface steps [64] lead to interaction energies of step pairs separated by a distance d (equivalent to our step-step distance) which also scale as d^{-2} in all cases where the last layer of the surface layer possess the same crystals structure as the bulk [65,66]. This case was called homoepitaxy by Houchmandzadeh and Misbah [67] which conceptually includes our domain wall case. The interaction typically follows weaker interaction laws ($\sim \ln d/d_0$) if the surface layer undergoes a reconstructive change, which we do not observe in ferroelastic domain walls. On the other hand, step meandering was advocated by Ref. [67] and has a clear equivalence in domain wall pattern formation when walls deviate from straight orientations. Wall bending effects were discussed in Refs. [15,26,68,69]. Meandering domain walls invokes possible additional symmetry breaking by the appearance of piezoelectricity in nominally high-symmetry phases [7]. Kinks in walls [70] have been simulated in other materials like high-T_c superconductors [25] and the mineral feldspar [71]. Extremely high kink concentrations which lead to macroscopic meandering was observed by transmission electron microscopy in $LiNbO_3$ [48] and it is likely that this configuration is also common in other uniaxial ferroelectrics. High kink concentrations tend to order or cluster the kinks inside the walls [48] so that it becomes useful to characterize the kink-kink interactions in Fourier space by their wave number. The wall self-energy obviously increases with increasing kink concentration, which is not considered here. We expand the interaction energy for small wave vectors q using the same dipole-dipole interaction as in wall modulations. This energy depends crucially on the phase between the kink-modulations in the two walls where the phase angle Φ describes the phase shift between two kink arrays. Following Houchmandzadeh and Misbah [67], the dipolar interaction energy per unit length of step $\Delta E \sim [1–d\ q\ K1(dq)\ \cos\ \Phi]/d^2$, where $K1$ is the modified Bessel function of the first order. The q dependence of the Bessel function was given in Ref [67]. to second order in q as $\Delta E \sim A(\cos\ \Phi)/d2 + 0.5(B - \ln\ (q^*d))q^2 \cos\Phi$, where A and B are numerical constants. The first term reproduces the d^{-2} scaling of the wall-wall interactions and depends on the position of the kinks with respect to each other but not on the modulation q vector. The second term depends explicitly on the modulation wave vector. The q dependence scales as $q^2 \ln\ q^*d$, which differs from the usual line tension of the wall which follows q^2. In kinked walls, the configuration $q \sim 1/d$ represents wall distances which are similar in magnitude to the average interkink distance in each wall. In this likely scenario the last term $\ln(qd)$ disappears and a simple q^2 dependence dominates the dispersion. The dispersion is positive or negative depending on the phase angle. This analysis demonstrates that the dipolar forces between two nonintersecting walls with several kinks lead not only to attraction or repulsion of the walls but also to a reshuffle of the kink patterns in the walls. Mobile kinks will minimize the energy by assuming a phase angle of π so that each kink is closest to an antikink. Fluctuations in the kink arrays follow, at least over some relevant parameter space, the usual parabolic dispersion so that one expects antiphase configurations with long-wavelength fluctuations.

All simulations were performed under open boundary conditions where the sample could change its shape. This approach makes the simulations much more realistic for most ferroelastic materials [11] and particularly the large group of disordered materials [72] where porosity often plays a major role [73]. Most ferroelastic minerals, for example, display porosities between 10% and 60% [68,74] which allows mineral grains to relax their shape when their microstructure changes as a function of temperature or pressure. The simulations highlighted that shapes changes occur for small enough samples when kinks are generated in a twin wall. Depending on the kink or antikink configuration, the sample bends in one direction or the opposite. The bents are restricted to a small area near the (anti-)kink position while the rest of the sample simply tilts in two opposite directions. The bent region is ∼10 lattice units wide; the sample tilts continue to the sample surface. In typical crystal structures like perovskites with lattice units of ∼0.4 nm or feldspars with 1.3 nm in the monoclinic b direction these bent regions are some 4–13 nm wide and are hence observable under the transmission electron microscope. The tilt angles are in the order of 1.2° for single kinks and are hence observable. This tilt angle is in the same order of magnitude as the twin angle of 2° in our simulations. The tilt becomes much greater for higher concentrations of tilts in the same orientation and could be seen even under the optical microscope. Kinks and antikinks will compensate the tilts and lead to a modulated twin wall. We have seen such modulated twin walls under the transmission electron microscope, but no analysis of possible kink formation was undertaken in our laboratory and none are known to the authors from literature.

ACKNOWLEDGMENTS

G.L. is grateful for the financial support by the Doctoral Starting Fund of Yantai University (Grant No. 1115–2222006). E.K.H.S. is grateful to EPSRC (EP/P024904/1) and the EU's Horizon 2020 programme under the Marie Sklodowska-Curie Grant (No. 861153).

[1] W. Eerenstein, N. D. Mathur, and J. F. Scott, Nature (London) **442**, 759 (2006).
[2] J. F. Scott, Science **315**, 954 (2007).
[3] G. Catalan, J. Seidel, R. Ramesh, and J. F. Scott, Rev. Mod. Phys. **84**, 119 (2012).
[4] E. K. H. Salje, X. Ding, Z. Zhao, T. Lookman, and A. Saxena, Phys. Rev. B **83**, 104109 (2011).
[5] E. K. H. Salje, J. Appl. Phys. **128**, 164104 (2020).
[6] S. Li, E. K. H. Salje, S. Jun, and X. Ding, Acta Mater. **125**, 296 (2017).
[7] O. Aktas, M. Kangama, G. Linyu, G. Catalan, X. Ding, A. Zunger, and E. K. H. Salje, Phys. Rev. Res. **3**, 043221 (2021).
[8] E. K. H. Salje, O. Aktas, M. A. Carpenter, V. V. Laguta, and J. F. Scott, Phys. Rev. Lett. **111**, 247603 (2013).
[9] E. K. H. Salje and M. A. Carpenter, Appl. Phys. Lett. **99**, 051907 (2011).

[10] J. F. Scott, Ferroelectrics **503**, 117 (2016).
[11] E. K. H. Salje, Annu. Rev. Mater. Res. **42**, 265 (2012).
[12] E. K. H. Salje and M. A. Carpenter, Physica Status Solidi B **252**, 2639 (2015).
[13] M. Foeth, A. Sfera, P. Stadelmann, and P. Buffat, Microscopy **48**, 717 (1999).
[14] D. Damjanovic, in *The Science of Hysteresis*, edited by G. Bertotti and I. D. Mayergoyz (Academic Press, Oxford, 2006), p. 337.
[15] E. K. H. Salje and Y. Ishibashi, J. Phys.: Condens. Matter **8**, 8477 (1996).
[16] T. Lookman, S. R. Shenoy, K. Ø. Rasmussen, A. Saxena, and A. R. Bishop, Phys. Rev. B **67**, 024114 (2003).
[17] K. Lee and S. Baik, Annu. Rev. Mater. Res. **36**, 81 (2006).
[18] X. He, S. Li, X. Ding, J. Sun, S. Kustov, and E. K. H. Salje, Acta Mater. **228**, 117787 (2022).
[19] X. Ding, O. Aktas, X. Wang, S. Li, Z. Zhao, L. Zhang, X. He, T. Lookman, A. Saxena, and J. Sun, J. Phys.: Condens. Matter **29**, 394002 (2017).
[20] E. K. H. Salje, S. Li, M. Stengel, P. Gumbsch, and X. Ding, Phys. Rev. B **94**, 024114 (2016).
[21] E. K. H. Salje, ChemPhysChem **11**, 940 (2010).
[22] J. Slutsker, Z. Tan, A. L. Roytburd, and I. Levin, J. Mater. Res. **22**, 2087 (2007).
[23] A. L. Roitburd, phys. stat. sol. (a) **16**, 329 (1973).
[24] G. Catalan, A. Schilling, J. F. Scott, and J. M. Gregg, J. Phys.: Condens. Matter **19**, 132201 (2007).
[25] D. A. Vul and E. K. H. Salje, Physica C **253**, 231 (1995).
[26] E. K. H. Salje, A. Buckley, G. van Tendeloo, Y. Ishibashi, and G. L. Nord, Am. Mineral. **83**, 811 (1998).
[27] G. Lu, S. Li, X. Ding, J. Sun, and E. K. H. Salje, Phys. Rev. Mater. **3**, 114405 (2019).
[28] Y. Deng, C. Gammer, J. Ciston, P. Ercius, C. Ophus, K. Bustillo, C. Song, R. Zhang, D. Wu, Y. Du *et al.*, Acta Mater. **181**, 501 (2019).
[29] A. G. Khachaturian, *Theory of Structural Transformations in Solids* (Courier Corporation, North Chelmsford, MA, 1983).
[30] N. A. Pertsev and E. K. H. Salje, Phys. Rev. B **61**, 902 (2000).
[31] J. Lajzerowicz and A. P. Levanyuk, Phys. Rev. B **49**, 15475 (1994).
[32] E. K. H. Salje and M. Vallade, J. Phys.: Condens. Matter **6**, 5601 (1994).
[33] S. Van Aert, S. Turner, R. Delville, D. Schryvers, G. Van Tendeloo, and E. K. H. Salje, Adv. Mater. **24**, 523 (2012).
[34] G. F. Nataf, M. Guennou, J. M. Gregg, D. Meier, J. Hlinka, E. K. H. Salje, and J. Kreisel, Nat. Rev. Phys. **2**, 634 (2020).
[35] E. K. H. Salje, S. Li, Z. Zhao, P. Gumbsch, and X. Ding, Appl. Phys. Lett. **106**, 212907 (2015).
[36] G. Lu, S. Li, X. Ding, and E. K. H. Salje, Appl. Phys. Lett. **114**, 202901 (2019).
[37] M. Zhang and D. Damjanovic, Smart Mater. Struct. **29**, 075012 (2020).
[38] S. Kustov, I. Liubimova, and E. K. H. Salje, Phys. Rev. Lett. **124**, 016801 (2020).
[39] M. L. Corró, A. el Hichou, E. Cesari, and S. Kustov, J. Phys. D **49**, 015001 (2015).
[40] A. M. Bratkovsky, S. C. Marais, V. Heine, and E. K. H. Salje, J. Phys.: Condens. Matter **6**, 3679 (1994).
[41] S. Marais, V. Heine, C. Nex, and E. Salje, Phys. Rev. Lett. **66**, 2480 (1991).
[42] K. Parlinski, E. K. H. Salje, and V. Heine, Acta Metall. Mater. **41**, 839 (1993).
[43] A. M. Bratkovsky, E. K. H. Salje, S. C. Marais, and V. Heine, Phase Transit. **55**, 79 (1995).
[44] E. K. H. Salje, X. Wang, X. Ding, and J. F. Scott, Adv. Funct. Mater. **27**, 1700367 (2017).
[45] Y. Yang, L. Zhang, S. Li, X. Ding, J. Sun, J. Weiss, and E. K. H. Salje, Phys. Rev. B **104**, 214103 (2021).
[46] Y. Yang, S. Li, X. Ding, J. Sun, J. Weiss, and E. K. H. Salje, Acta Mater. **195**, 50 (2020).
[47] X. He, S. Li, X. Ding, J. Sun, S. M. Selbach, and E. K. H. Salje, Acta Mater. **178**, 26 (2019).
[48] J. Gonnissen, D. Batuk, G. F. Nataf, L. Jones, A. M. Abakumov, S. Van Aert, D. Schryvers, and E. K. H. Salje, Adv. Funct. Mater. **26**, 7599 (2016).
[49] A. S. Everhardt, S. Damerio, J. A. Zorn, S. Zhou, N. Domingo, G. Catalan, E. K. H. Salje, L.-Q. Chen, and B. Noheda, Phys. Rev. Lett. **123**, 087603 (2019).
[50] W. Selke, Phys. Rep. **170**, 213 (1988).
[51] A. L. Roitburd, phys. stat. sol. (a) **37**, 329 (1976).
[52] I. A. Luk'yanchuk, A. Schilling, J. M. Gregg, G. Catalan, and J. F. Scott, Phys. Rev. B **79**, 144111 (2009).
[53] N. A. Pertsev, J. Novak, and E. K. H. Salje, Philos. Mag. A **80**, 2201 (2000).
[54] G. Lu, S. Li, X. Ding, J. Sun, and E. K. H. Salje, npj Comput. Mater. **6**, 145 (2020).
[55] S. Nosé, J. Chem. Phys. **81**, 511 (1984).
[56] W. G. Hoover, Phys. Rev. A **31**, 1695 (1985).
[57] S. Plimpton, J. Comput. Phys. **117**, 1 (1995).
[58] A. Stukowski, Modell. Simul. Mater. Sci. Eng. **18**, 015012 (2009).
[59] W. T. Lee, E. K. H. Salje, L. Goncalves-Ferreira, M. Daraktchiev, and U. Bismayer, Phys. Rev. B **73**, 214110 (2006).
[60] See Supplemental Material at http://link.aps.org/supplemental/10.1103/PhysRevB.106.144105 for the lattice distortion of simple twin structure without atomic kink inside the horizontal twin wall.
[61] R. V. Kukta and K. Bhattacharya, J. Mech. Phys. Solids **50**, 615 (2002).
[62] K. H. Lau and W. Kohn, Surf. Sci. **65**, 607 (1977).
[63] S. Li, U. Bismayer, X. Ding, and E. K. H. Salje, Appl. Phys. Lett. **108**, 022901 (2016).
[64] G. Lu, S. Li, X. Ding, J. Sun, and E. K. H. Salje, Sci. Rep. **9**, 15834 (2019).
[65] L. E. Shilkrot and D. J. Srolovitz, Phys. Rev. B **53**, 11120 (1996).
[66] A. F. Andreev and Y. A. Kosevich, JETP **81**, 1435 (1981).
[67] B. Houchmandzadeh and C. Misbah, J. Phys. I France **5**, 685 (1995).
[68] E. K. H. Salje, Minerals **11**, 478 (2021).
[69] Y. Yang, S. Li, X. Ding, J. Sun, and E. K. H. Salje, Adv. Funct. Mater. **26**, 760 (2016).
[70] L. Zhang, S. Li, X. Ding, J. Sun, and E. K. H. Salje, Appl. Phys. Lett. **116**, 102902 (2020).
[71] I. Tsatskis and E. K. H. Salje, Am. Mineral. **81**, 800 (1996).
[72] E. K. H. Salje and K. A. Dahmen, Annu. Rev. Condens. Matter Phys. **5**, 233 (2014).
[73] B. Casals and E. K. H. Salje, Phys. Rev. E **104**, 054138 (2021).
[74] E. K. H. Salje, AIMS Mater. Sci. **9**, 1 (2022).